Title:

Seasonal variation of earthquake source characteristics of the long-duration Palghar swarm, western India

Authors:

Himangshu Paul[1,2], Sunilkumar T.C. and M. Shekar[1]

Corresponding author Email:

heman2007@gmail.com

Affiliation:

[1]CSIR-National Geophysical Research Institute, Hyderabad-500007, India

[2]AcSIR-Academy of Scientific and Innovative Research, Ghaziabad, India

Journal submission status:

This paper has been submitted to ***Tectonophysics*** for peer review.

Seasonal variation of earthquake source characteristics of the long-duration Palghar swarm, western India

Himangshu Paul[1,2*], Sunilkumar T. C.[1], and Shekar M.[1]

[1]CSIR-National Geophysical Research Institute, Uppal Road, Hyderabad, India

[2]Academy of Scientific and Innovative Research (AcSIR), Ghaziabad, India

*Corresponding author e-mail: heman2007s@gmail.com

Highlights

- Moment tensor inversion, stress inversion and source parameters of the largest earthquake in the Palghar swarm are estimated
- Overall, the prevalence of normal faulting along N-S-oriented, steeply-dipping planes are observed
- Low static stress drops of ~ 2 MPa and high non-DC components (~42%) are observed
- A subtle but consistent seasonal variation in the source characteristics is observed
- Pure normal faulting observed during the post-monsoon is influenced by the regional convergent stress regime during summer

Abstract

A swarm sequence initiated in November 2018 in the Palghar region near the western coast of India, and continued with high intensity for two years. About 8300 earthquakes were found with horizontal and depth uncertainties of ≤ 1.5 km after relocation. The earthquakes were distributed along two narrow N-S oriented clusters, separated by ~5 km. We performed time-domain regional waveform full moment tensor inversion to compute focal mechanisms of the 33 $M_L \geq 3.5$ earthquakes, followed by stress inversion. Source parameters for 28 of these events were estimated from frequency spectra analysis. The focal mechanisms indicate dominant normal faulting along steeply dipping, N-S-oriented nodal planes, with high non-DC components (~42%). Stress inversion also reveals a normal-faulting regime, in contrast to the regional India-Eurasia compressive stress regime. The Palghar swarm has been previously linked to rainfall, and our results also show contrasting earthquake source properties during the post-monsoon period, when cumulative rainfall is highest, compared to summer. During the post-monsoon period, the strikes are strictly N-S, slips are ~-100°, and a pure normal-faulting regime is observed, accompanied by increased non-DC components and reduced static stress drops. In contrast, during the summer season, oblique-normal faulting occurs along NNE-SSW-oriented planes, with slip angles reduced to about -65°. We infer that pure normal faulting induced by vertical rainwater load during the post-monsoon transitions to a combination of regional convergent stress regime and vertical loading due to remnant water during summer, resulting in oblique normal faulting. This interplay possibly sustains the rain-induced swarm.

Keywords

Rainfall-induced seismicity, Post-monsoonal loading, Focal mechanism, Normal faults, Source parameters, Stress Inversion.

1 Introduction

On the west coast of India, about 100 km north of the city of Mumbai, a swarm sequence initiated in November 2018 in the Palghar region and continued until the end of 2020 with high intensity (Fig. 1), after which the intensity decreased significantly. Palghar is located within the Deccan Volcanic Province (DVP), an upper Cretaceous flood basalt covering a large part of western India. Prior to the earthquake swarm, no seismicity was reported in the Palghar region. Generally, earthquake swarms denote a large number of small to moderate magnitude earthquakes with no identifiable main shock within a relatively small volume [Mogi, 1963]. The swarm sequences are, in general, observed in areas of volcanic and geothermal activity [Hill, 1977; Shelly et al., 2013], where the crustal part is highly fractured, and the stress fields are exceptionally heterogeneous. In such an environment, very minimal shear stress is needed to produce seismogenic dislocations, resulting in a large number of small events with few or no larger ones [Mogi, 1963]. In addition to volcanic and hydrothermal processes, swarms can also occur through fluid diffusion [Shapiro et al., 1997] and aseismic creep [Lohman and McGuire, 2007]. In a few cases, it is seen that the fluid content generates tensile or hybrid shear-tensile fractures, which are reflected by non-double-couple focal mechanisms [Dreger et al., 2000], whereas in others, fluids trigger shear failure [Sibson, 2003].

Despite absence of active volcanism or hydrothermal sources, the Indian Shield region has witnessed several earthquake swarms (Fig. 1 inset), including the Khandwa/Bamhori (Madhya Pradesh) swarm in 1993-1994, 1998-1999 and 2000 [Srivastava and Dube, 1996], Jawhar (Maharashtra) swarm during 1994, 2012 and 2018; Valsad/Navasari (southern Gujarat) swarms in 1986-1987 and 2016-2017 [Rao et al., 1991; Sateesh et al., 2019], and Talala (Saurashtra, Gujarat) swarm in 2001, 2004, 2007 and 2011 [Hainzl et al., 2014]. Most of these swarm sequences are located within the vicinity of major reservoirs/dams. Among these, a clear connection between rainfall and reservoir has been observed for the swarms in Talala [Hainzl et al., 2014; Singh and Mishra, 2015] and Navsari/Valsad regions [Sateesh et al., 2019]. In addition, short-duration (1-3 months) earthquake sequences occurring coincidentally with monsoonal rain, in the absence of a nearby reservoir or dam, have also been reported from some parts of India [Raju et al., 2000; Chopra et al., 2008; Wadhawan et al., 2021]. There is no volcanic/thermal source or major reservoir near the Palghar swarm. In contrast, the role of rainfall in causing seismicity in Palghar is clearly demonstrated from recent studies [Sharma et al, 2020; 2023; Paul et al., 2024; Paul and Shekar, 2026]. However, earthquake sequences induced solely by rainfall are short-lived, as seen both in India [Raju et al., 2000; Wadhawan et al., 2021] and globally [Hainzl et al., 2006; Husen et al., 2007]. The long-duration Palghar swarm induced by rainfall is enigmatic and requires thorough investigation. Studying this swarm is also important from a hazard perspective, as even a moderate-magnitude earthquake in a stable continental region (SCR) can cause extensive damage due to the generally minimal attenuation of seismic energy with distance in plate interiors [Johnston, 1996; Calais et al., 2016].

Source characteristics and the prevailing stress field play a key role in elucidating the crustal deformation geometry and seismogenesis of a region. The India-Eurasia convergence acts as the dominant stress driver for seismogenesis across much of the Indian subcontinent. In the case of Palghar, where rainfall appears to have triggered a long-duration swarm, it becomes particularly important to examine whether the source processes deviate from the existing stress regime. In this study, we analyse the largest earthquakes ($M_L \geq 3.5$) within the swarm sequence, estimate their focal mechanisms, and determine the prevailing stress field. Source parameters of these earthquakes are calculated to constrain fault dimensions and stress drops, thereby offering a window into the mechanics of swarm generation. We then observe the temporal variation of source characteristics, especially during the summer and post-monsoon seasons. Together, these observations may provide a better understanding of the seismogenic behaviour of the Palghar intraplate swarm and, more broadly, the processes governing earthquake swarms in stable continental regions.

2 Data

Council of Scientific and Industrial Research – National Geophysical Research Institute (CSIR-NGRI) started deploying broadband seismic stations around the source region immediately after the initiation of earthquake activities in November 2018 (Fig. 1). The complete network of six broadband stations became operational from January 2019. Each of the seismic stations is equipped with either Güralp CMG-3C or Reftek-151 sensors along with a 24-bit Reftek-130 data recorder. Data are recorded at 100 samples per second in continuous mode and are transmitted to the CSIR-NGRI seismological observatory at Hyderabad in near real-time. Accurate time-tagging of the order of microseconds is obtained through GPS synchronisation. The stations adequately cover the source region azimuthally, and their distance from the source region is optimal [Srinagesh et al., 2020]. For this study, the earthquakes recorded in the Palghar network between February 2019 and November 2020 are utilised.

3 Methods

3.1 Computing Earthquake Locations

In general, earthquake location error mostly arises due to the failure in picking arrival-time phases accurately or due to an inconsistent velocity model. We have used the 1D velocity model of Paul et al. [2024], who have performed several synthetic tests to demonstrate that their velocity model is adequate for the region. To account for the inaccuracy in phase picking, we have employed the nonlinear probabilistic location program NonLinLoc [Lomax et al., 2000]. NonLinLoc associates a Gaussian error with phase-picking inaccuracy and travel-time errors due to minute velocity variations and converts them into location errors. By discarding earthquakes with large location errors, a set of well-located earthquakes with consistent input parameters is obtained. This methodology has been proven to be effective in obtaining reliable sets of earthquakes with precise locations in a variety of intraplate seismic zones across India [Gahalaut et al., 2023; Paul et al., 2021; 2025]. Hence, we used NonLinLoc and the velocity model of Paul et al. [2024] to relocate all earthquakes recorded in the CSIR-NGRI network from February 2019 to November 2020. For NonLinLoc, the 1D velocity model is expanded into a 3D grid – 80 kms in the north-south and east-west directions and 40 km in the downward vertical direction, with the centre of the grid at 20.10°N and 72.90°E. The grid node separation is 100 m in all directions. The grid node with the highest probability is considered the best location of an event. The grid is efficiently searched by the Oct-tree Importance sampling algorithm. The local magnitude (M_L) is calculated using the relation of Hutton and Boore [1987], with amplitudes scaled to account for the attenuation characteristics of Palghar [Subhadra and Shekar, 2024].

3.2 Moment Tensor and Stress Inversions

Focal mechanisms provide crucial insights into earthquake processes and seismotectonics. In this study, we estimated focal mechanisms for 33 earthquakes with $M_L \geq 3.5$ that occurred between February 2019 and November 2020. We employed the time-domain regional waveform full moment tensor inversion technique of Herrmann [2013] for this analysis. For preprocessing, vertical, radial, and transverse component ground displacement were truncated to 10 seconds before and 180 seconds after the P wave arrival. Then these seismograms were filtered using a Butterworth band-pass filter in the frequency range 0.03-0.3 Hz, which was tuned differently for individual events. The Green functions were computed using the 1-D crustal velocity model of Paul et al. [2024] for each source-receiver distance. The grid search for strike, dip, and rake was performed over the entire range and source depth, from 0 to 30 km, in steps of 1 km. The fitting between observed and synthetic waveforms was minimized in the least-squares sense. In general, the best fitting waveform was determined by the lowest weighted variance reduction, with each trace weighted as a function of epicentral distance [Herrmann, 2013]. The resulting full moment tensor solutions were decomposed into the isotropic (ISO) and deviatoric components following Vavryčuk [2015]. The deviatoric component is further composed of the compensated linear vector dipole (CLVD) and double-couple (DC) parts. The inversion scheme for a few earthquakes is shown in Fig. S1 (Supplementary Material).

Focal mechanism solutions were inverted to reconstruct the local stress field within the study area. The analysis was carried out using a modified implementation of the STRESSINVERSE software package (Vavryčuk, 2014). This tool employs an iterative joint inversion technique based on Michael's linear method [Michael, 1984], which simultaneously estimates the stress tensor and identifies the most compatible fault orientations based on the Mohr-Coulomb criterion [Vavryčuk, 2011; Vavryčuk, 2014]. This is especially valuable when focal mechanisms involve uncertainties in strike, dip, or rake angles. The inversion provides the principal stress (σ_1, σ_2, and σ_3) directions, shape ratio ($R = \frac{\sigma_1 - \sigma_2}{\sigma_1 - \sigma_3}$) and stress ratio ($\varphi = 1 - R$). To test the stability of the results and to quantify their uncertainty, 1000 bootstrap realizations were incorporated in the inversion, each generated by adding random perturbations to the input focal mechanisms and also varying the co-efficient of friction between 0.4 and 1. R and φ vary between 0 and 1. Anderson's faulting parameter, $A_\varphi = (n + 0.5) + (-1)^n(\varphi - 0.5)$ [Simpson 1997], gives the prevailing faulting regime. Here, n indicates how many principal stresses exceed the vertical stress. The parameter A_φ ranges from 0 to 1 for normal faulting, 1 to 2 for strike-slip faulting, and 2 to 3 for reverse (thrust) faulting [Hardebeck and Hauksson, 2001]. All the 33 estimated focal mechanism solutions were utilized for stress inversion.

3.3 Estimation of Source Parameters

Earthquake source parameters such as seismic moment, stress drop, and fault radius may provide additional insights into the Palghar seismogenesis processes. Spectral analysis using the Python-based SourceSpec package [Satriano, 2023] was employed for estimating basic source parameters, following the approach depicted in Paul et al. [2025]. At first, frequency spectra were computed from 5-second S-wave displacement windows obtained from horizontal (N and E) components, and a root mean square (rms) spectrum was calculated from them (Fig. S2). Noise spectra from equi-length pre-signal windows from each component, as well as an rms noise spectrum, were computed for comparison. The theoretical spectrum, computed by SourceSpec using a simple rupture model [Brune, 1970], is fitted with the observed rms spectrum to invert for the corner frequency (f_c) and spectral flat level (Ω_0). However, the ground motion at a given distance is always a combined effect of the source, wave propagation, and site contributions. The average difference between theoretical spectra and observed spectra across several events for a particular station was taken as the site response, which was then removed from the observed spectra. To account for path effects, the observed spectra were corrected for travel-time-dependent attenuation using the attenuation relation for Palghar [Subhadra and Shekar, 2024]. Since the Palghar earthquakes are confined within a narrow depth range (0-10 km), depth-dependent attenuation is not likely to play a significant role. The theoretical frequency (f) spectrum corrected for attenuation and site effects is given by

$$\Omega_0(f) = \frac{F_S R_\theta}{4\pi\rho R\beta^3} . \frac{M_0}{1 + \left(\frac{f}{f_c}\right)^2} \cdots\cdots (1)$$

where M_o is seismic moment, f_c is corner frequency, R_θ is the radiation pattern effect, generally taken to be 0.6, F_S accounts for the free-surface effect, taken to be 2, ρ is density, β is shear wave velocity at the source region, and R is epicentral distance and accounts for the geometrical spreading effect.

Following Eshelby [1957], the source radius r and uniform stress drop (Δσ) can be calculated from M_o (equivalent to Ω_0) and f_c as:

$$r = \frac{2.34\beta}{2\pi f_c} \cdots\cdots (2)$$

$$\Delta\sigma = \frac{7}{16}\frac{M_0}{r^3} \cdots\cdots (3)$$

We determined the source parameters of 27 (out of 33) earthquakes with $M_L \geq 3$.. The f_c could not be constrained within satisfactory level of uncertainty for the rest of the events (6). The scheme for inverting the corner frequency and spectral flat level by fitting the source spectra is shown for selected events in Fig. S2.

4 Results

More than 10000 earthquakes were recorded in the CSIR-NGRI network between January 2019 and November 2020, with M_L varying from -0.1 to 4.6. However, the number of earthquakes with horizontal (Δx) and depth uncertainty (Δz) ≤ 1.5 km was 8377. The 1.5 km bounds were found to be optimal for earthquakes in the Indian intraplate regions [Paul et al., 2021; Gahalaut et al., 2023]. We performed all analyses with the well-located events only. The earthquakes are seen to be tightly distributed in two N-S-oriented clusters, with more than 98% of the earthquakes confined within the first 10 km of the crust (Fig. 1). We designate them as east and west clusters, which are separated by ~5 km. The earthquakes in Palghar (west cluster) were reported to start in November 2018 [Sharma et al., 2020], while the east cluster initiated around November 2019. The temporal variation of seismicity indicates its non-stationary nature, with along-strike migration between the two clusters at different times, particularly during the initiation of the east cluster (November 2019) and during October-November 2020 (Fig. 1a). The east and west clusters individually span about 18 and 22 km in the N-S direction, respectively, with a combined extent of ~30 km (Fig. 1b). In a cross-section along the E-W direction, the seismicity is strictly constrained to two near-vertical planes, each ~2 km thick (Fig. 1c). There is no depth migration with time, as the seismicity depth (~12 km) attained in the first few months (by May 2019) is not exceeded thereafter (Fig. 1b).

Focal mechanism solutions of the 33 well-recorded events ($M_L \geq 3.5$) by MT inversions are presented in Fig. 2 and Table S1 (Supplementary Material). The majority of the earthquakes show pure normal faulting mechanisms, along with a few earthquakes that show normal mechanisms with a minor strike-slip component (Fig. 2a). The orientations of the nodal planes are primarily along ~N-S (between NNW-SSE and NNE-SSW), and they are dipping steeply (55°-75°) (Fig. 2b). The rake shows a bimodal distribution with peaks at -65° (oblique-normal) and -100° (normal). The decomposed isotropic (ISO), compensated linear vector dipole (CLVD), and double couple (DC) components reveal significant non-DC (ISO + CLVD) contributions (Table S1). On average, the DC component accounts for about 58% of the MT, while CLVD and ISO contribute ~24% and ~18%, respectively. The stress inversion results obtained from 33 focal mechanisms are shown in Fig. 3a-c and Table S2. The P-axis (pressure axis) for most events is plunging steeply (average 65°), while the T-axis (tension axis) is oriented E-W with a gentle plunge (~22°) (Fig. 3a). Overall, the trend and plunge of the principal stresses (with 95% confidence level) show that σ_1 plunges near-vertically (79°), while σ_2 and σ_3 are near-horizontal (plunge 10° and 6°) oriented N-S and E-W, respectively (Fig. 3a,c). The resultant R value of 0.60 and the 3D Mohr circle representation (Fig. 3b) indicate a tri-axial stress field. In the Mohr circle representation, the majority of the nodal planes lie close to the σ_1 - σ_3 circle, indicating that slip occurs on planes controlled mainly by σ_1 and σ_3. The estimated A_φ of 0.40 (Table S2) implies a dominant normal stress regime [Simpson, 1997].

The estimated source parameters, including source radius (r), seismic moment (M_o), moment magnitude (M_W), and static stress drop ($\Delta\sigma$) for 27 earthquakes, are listed in Table S3. If the source parameters of an earthquake depend on its size, this is termed source scaling. Previous studies have reported both source scaling [Trugman and Shearer, 2017] as well as scale invariance [Hardebeck and Aron, 2009]. The source parameters from the 27 earthquakes are plotted against one another (Fig. 3d-f) to examine their relationships. Under scale invariance, the relation $M_o \propto f_c^{-3}$ must be satisfied [Aki, 1967], whereas self-similarity scaling is not followed if $M_o \propto f_c^{-(3+\varepsilon)}$ [Kanamori and Rivera, 2004], where ε is a small positive number. For the Palghar sequence, M_o ranges from 3.36×10^{13} Nm to 1.37×10^{15} Nm, and $M_o \propto f_c^{-(3+0.6)}$ provides a better fit to the observed data than f_c^{-3} (Fig. 3d). Similarly, the source radii vary from 232 m to 508 m, and the relation $M_o \propto r^{3.48}$ yields a higher regression coefficient than $M_o \propto r^3$. The estimated stress drops range between 0.7 and 4.9 MPa, with a median of 1.85 MPa, and $M_o \propto \Delta\sigma^{1.48}$ provides a good fit to the data. These observations may indicate that self-similarity scaling is not followed in the case of Palghar earthquakes. A similar breakdown in self-similarity scaling has been reported for reservoir-induced seismicity in the Koyna region (~300 km south of Palghar) [Mahato, 2024]. However, the relatively small number of events in our study does not allow for a conclusive statement regarding source scaling in the Palghar region. Moreover, rupture complexity, repeated failure of the same fault segment, dynamic weakening, or processes involving fluids, pore pressure variation, and aseismic slip may contribute to such deviations [Brodsky and Kanamori, 2001; Fischer and Hainzl, 2017; Trugman and Shearer, 2017; Mahato, 2024].

5 Discussion

5.1 The role of rainfall in the seismogenesis of the Palghar swarm

Generally, the summer monsoon begins in June and lasts until September across most parts of India, during which about 80% of the annual rainfall occurs [Kulkarni, 2012]. The plot of seismicity with rainfall indicates that seismicity frequency increases toward the end of the monsoon season, around November, when cumulative rainfall is highest (Fig. S3). In this study, we refer to this period as the post-monsoon. The time delay between the rainfall peak and seismicity peak is about 30-90 days, which is typical of fluid-induced seismicity [Talwani et al., 2007]. Over the course of the Palghar swarm, distinct stages of swarm evolution have been observed in this post-monsoon period – the swarm was reported to initiate during November 2018 [Sharma et al., 2020], the east cluster of seismicity first appeared in November 2019, and in November 2020, seismicity migrated extensively toward the northern and southern extremities of the clusters, effectively extending the seismic zone (Fig. 1). The increased seismic moment during the post-monsoon period [Sharma et al., 2020; Paul and Shekar, 2026], together with the occurrence of the largest earthquake of the swarm in December 2019 (Table S3), confirms enhanced seismogenesis during this period.

Gahalaut et al. [2022] reported that pore pressure induced by time-varying rainfall extends to depths of 6-8 km with sufficient magnitude to trigger earthquakes at those depths. The velocity structures estimated by recent studies for the seismic zone [Paul et al., 2024; Kanaujia et al., 2025] reveal a relatively low shear-wave velocity (V_S) and a high V_P/V_S ratio, along with high crack density and saturation [Singh et al., 2026]. These seismic properties are generally associated with the presence of fluids [Nur and Simmons, 1969; Popp and Kern, 1994]. Moreover, earthquake location errors were seen to increase during post-monsoon seasons when a constant V_P/V_S ratio was applied, and the ratio had to be increased to reduce these errors [Paul et al., 2024], clearly establishing that high V_P/V_S is linked to rainfall. Seismicity tightly confined to steep planes (Fig. 1c) possibly reflects pre-existing faults or planes of weakness. Paul and Shekar [2026] observed localised concentrations of earthquakes along these planes during the post-monsoon season. Sharma et al. [2023] proposed that fluids percolated through multiple channels near the surface, forming a network of cracks and fissures to the permeable (fault) zone. Pore pressure gradually increasing in the fault zone ultimately resulted in seismicity. All of the above observations strongly support the role of rainfall in Palghar seismogenesis.

5.2 Seasonal modulation of source characteristics

The dominant stress regime within India arises from the ongoing northeastward convergence between the Indian and Eurasian plates. Regions governed by this stress regime typically exhibit either thrust motion along ~E-W oriented faults [Rajendran et al., 2017] or strike-slip motion along ~N-S oriented faults [Paul et al., 2015; Sunilkumar et al., 2019]. Normal-faulting earthquakes are observed only when this convergent regime is locally modified by other stress influences, like in the case of reservoir-triggered seismicity in the Koyna-Warna region [Gupta, 2002; Gahalaut and Singh, 2004] or in certain segments of the Indo-Burma subduction zone [Earnest et al., 2021]. In the case of Palghar, the majority of the nodal planes are oriented ~N-S, and the seismicity clusters also align in the N-S direction (Fig. 2). Sharma et al. [2020] indicated the presence of various N-S striking lineaments within the region of study, some of which might be linked to faults. This could indicate that these earthquakes occurred on one or several ~N-S trending faults. Focal mechanism solutions and stress inversion results consistently point to a dominant normal-faulting regime. InSAR analysis during the initiation of the Palghar swarm (November 2018 to May 2019) also showed a ~3 cm subsidence of the source region [Sharma et al., 2020]. These observations indicate a local modification of the India-Eurasia convergent stress regime to a normal-faulting regime in the Palghar region.

If the source results are analysed by separating the data into two groups – one covering the summer (including monsoon) season (May to October) and the other the post-monsoon period (November to April) - a slight but consistent modification in the source characteristics is observed. During the summer, the strikes of the nodal planes are mainly oriented in the NNE-SSW direction, with slips showing oblique-normal motion (Fig. 4a). In contrast, during the post-monsoon, the strikes shift to N-S to NNW-SSE orientations, and slips exhibit dominant pure normal motion (Fig. 4b). The dips of the nodal planes remain broadly consistent across seasons. The average double-couple component decreases, while isotropic and CLVD components increase during the post-monsoon compared to the summer (Fig. 4c). Similarly, pressure axes show a mixed distribution of steep, intermediate and gentle plunges during May-October, whereas dominantly steep plunges are observed in the post-monsoon (Fig. 5a,d). The scattered nodal planes within the Mohr circle representation during May-October indicate that a few slips occur on planes controlled by σ_2 and σ_3, in addition to those governed by σ_1 and σ_3; whereas in the post-monsoon, slip occurs on planes controlled by σ_1 and σ_3 only (Fig. 5b,e). The stress inversion results show that σ_1 plunges near-vertically (86°) during the post-monsoon compared to a moderate plunge (63°) in summer (Fig. 5c,f, Table S2). In contrast, the plunge of σ_2 increases (26°) during the summer compared to post-monsoon (4°), while the plunge of σ_3 remains similar across seasons. Although we expect a smooth transition of the source properties from the dry season to the post-monsoon season with the onset of monsoon, we do not observe it, possibly due to the smaller number of events or the inherent uncertainties in the estimation of source properties.

From the above results, it is clear that near-vertical σ_1 and horizontal, E-W-oriented σ_3 during the post-monsoon period promote faulting with strikes along the N-S direction and slip by pure normal motion (rake -90°). The cumulative rainfall reaches its peak at the end of the monsoon season (Fig. S3), which may be locally trapped or injected into permeable zones through a network of fissures [Sharma et al., 2023]. This accumulated rainwater likely acts as the vertical load, facilitating pure normal motion. In addition, fluid injection is often accompanied by aseismic deformation [De Barros et al., 2019]. The static stress drops for the entire duration of the Palghar swarm were found to be low (average 2.2 MPa) compared to other peninsular Indian earthquakes [Baumbach et al, 1994; Antolik and Dreger, 2003; Paul et al., 2025]. The temporal variation of Palghar source parameters indicates a further decrease in static stress drop, along with seismic moment, during the post-monsoon season, while the source radii are not significantly affected by seasons (Fig. 6). Therefore, the average static stress drop during post-monsoon can be considered equivalent to effective stress drop ($\Delta\sigma_c$). A low $\Delta\sigma_c$ can be an indication of aseismic deformation [Fischer and Hainzl, 2017; Danré et al., 2022]. Moreover, Paul and Shekar [2026] showed increased b-value and gradually-varying earthquake frequency associated with cataclastic (aseismic) deformation during the post-monsoon. A mismatch between slip estimated from earthquake seismic moment and InSAR deformation [Gahalaut et al., 2022], together with increased non-DC components during post-monsoon (Fig. 4c, Table S1), also supports the existence of aseismic deformation. Since both the west and east clusters were initiated during post-monsoon seasons of different years, the collapse of substructures together with aseismic deformation under the combined influence of accumulated rainwater load and gravity appears to explain the local modification to a pure normal-faulting regime from a convergent stress regime.

Through the winter (dry season) and by the onset of summer, the accumulated water load is expected to reduce. Consequently, the regional stress regime (India-Eurasia convergence) likely begins to influence the fault system as strikes orient NNE-SSW, slips become oblique-normal, non-DC components become relatively small (Fig. 4), and P-axes orientations are more widely distributed (Fig. 5a). If a pure normal stress regime is influenced by the NE-SW-oriented convergent stress regime, σ_1 may slightly tilt toward the SW from vertical as NE compression increases, σ_2 steepens while σ_3 remains largely unchanged. This is precisely what the stress inversion results indicate for earthquakes during May-October (Fig. 5c, Table S2). To further prove this point, we combined focal mechanism solutions from the post-monsoon period (November-April) with those from a region dominated by the India-Eurasia convergent stress regime and performed stress inversion (following Section 3.2). The latter dataset was obtained from upper crustal earthquakes in the Sikkim region [Sunilkumar et al., 2019], where the majority of the faults are oriented ~N-S and motion is dominated by strike-slip mechanisms. Stress inversion results from this combined dataset yield P-T-axis orientations, Mohr circle representations, and principal axis trends and plunges that are almost identical to those obtained from May-October earthquakes (Fig. 5, Fig. S4, Table S2). This implies that in May-October, the earthquakes are controlled by the combined influence of the regional convergent stress regime and the localised normal-faulting regime. This combined influence likely sustains seismicity during the summer. During the post-monsoon, the water load again leads to the dominating pure normal-faulting regime and pure normal earthquakes. Such an interplay of mechanisms likely explains the longevity of the rainfall-induced seismogenesis in Palghar.

6 Conclusions

More than 10000 earthquakes occurred in the Palghar swarm over a two-year period, of which about 33 events had local magnitude $M_L \geq 3.5$. In this study, we conducted a holistic investigation of the source characteristics, including hypocentre relocation, moment tensor inversion, stress field inversion, and computation of source parameters. The seismicity is distributed along two N-S-oriented, steeply dipping planes separated by ~5 km. Overall, we observe a prevalence of normal-faulting earthquakes with ~N-S strikes and steep dips. About 42% non-DC components are observed in the region. Stress inversion also indicates a pure normal-faulting regime, with a near-vertical maximum principal axis σ_1 and near-horizontal σ_2 and σ_3 oriented north and east, respectively. The corner frequency, static stress drop, and source radius appear to scale with seismic moment. Low static stress drop values suggest the possible presence of aseismic deformation.

This study, together with previous work, strongly confirms the role of rainfall in the seismogenesis of the Palghar swarm. Seismicity frequency is seen to increase as the rainfall intensity peaks, with a lag. Important stages of the swarm evolution, such as the initiation of the swarm (west cluster), activation of the east cluster and seismicity migration in the N-S direction, seem to be associated with the post-monsoon period, when cumulative rainfall is high. Analyses of the source characteristics before and after the rain reveal key differences. During the post-monsoon period, pure normal faulting along strictly N-S-oriented faults is observed, accompanied by higher non-DC components. The P-axes and σ_1 are vertical during this period, while static stress drops and seismic moments decrease significantly. In contrast, during the summer season, oblique normal faulting occurs along NNE-SSW-oriented faults. The P-axes show a mixed distribution of steep, intermediate and gentle plunges, whereas the plunge of σ_1 is reduced, and σ_2 steepens from horizontal. The results imply that, during the post-monsoon, the accumulated water load leads to the collapse of substructures and possibly aseismic deformation, locally modifying the regional convergent stress regime into a pure normal-faulting regime. As the water load gradually dissipates, the regional stress regime reasserts dominance, shifting faulting style from pure-normal to oblique-normal. This interplay between rainfall-induced loading and the regional stress regime sustains seismicity and explains the long-duration nature of the Palghar swarm.

Figure Captions

Figure 1: Plot of the Palghar seismicity in (a) map view, (b) cross-section along the N-S profile Y-Y' and (c) cross-section along the E-W profile X-X'. The seismicity is colour-coded by time, with each colour representing approximately 4-months of activity. In (a), seismic stations are shown as green triangles. The inset map of India is displayed in the lower right. Locations of a few past swarms within India are shown as yellow ovals in the inset and labelled. N-Navsari, T-Talala, B-Bamhori, H-Hyderabad. The red square represents the study region.

Figure 2: (a) Double-couple focal mechanisms of the Palghar swarm, along with seismicity, are shown on the topography map. Both seismicity and focal mechanisms are colour-coded by depth. Serial numbers corresponding to the focal mechanism solutions in Table S1 (Supplementary) are labelled beside the beach-ball diagrams. (b) Rose-plot distributions of strike, dip and rake from the focal mechanism solutions are shown.

Figure 3: Stress inversion and source parameter results obtained from all $M_L \geq 3.5$ earthquakes of the Palghar swarm. (a) Azimuthal plot of Pressure- (red circles) and Tension-axes (blue + symbols) from focal mechanisms, shown along with the orientation of principal stresses, (b) 3D Mohr circle representation of the principal stresses, with normal stress increasing along the x-axis and shear stress increasing along the y-axis. The diameter of the large circle is σ_1 - σ_3, and the two inner circles meet at σ_2, where σ_1, σ_3, and σ_2 are the maximum, minimum and intermediate principal stresses. The blue + symbols represent individual nodal planes. (c) Inverted principal stress axes

(with 95% confidence interval) shown in lower-hemisphere projection. Plots of (d) corner frequency vs seismic moment, (e) source radius vs seismic moment, and (f) static stress drop vs seismic moment are shown as red diamond symbols. Dashed black lines in (d), (e) and (f) represent scale-invariance for fixed static stress drops, whereas dashed green lines represent scale-dependence.

Figure 4: Rose-plot distributions of strike, dip and rake from focal mechanisms during (a) May to October and (b) November to April. (c) Plot of the double-couple (DC, diamond symbol), compensated linear vector dipole (CLVD, circle), and isotropic (ISO, square) components of the focal mechanism solutions as a function of time (June to December 2019). Individual values are shown as open symbols, while mean values (with standard deviation) are larger filled symbols. Quantities during summer (including monsoon) are indicated in sky blue, whereas those during the post-monsoon are in deep blue. The x-positions of the mean values are unrelated to time and are plotted in this way for visual convenience. Daily rainfall (obtained from the NASA repository, https://giovanni.gsfc.nasa.gov/giovanni) is plotted as pink histograms.

Figure 5: Stress inversion results separated for focal mechanisms during May to October and November to April. (a), (d) Azimuthal plots of P- and T-axes, along with the orientation of principal stresses. (b), (e) 3D Mohr circle representations of the principal stresses. (c), (f) Inverted principal stress axes (with 95% confidence interval) shown in lower-hemisphere projection. For interpretation of the various colours and symbols, refer to the captions of Fig. 3(a), 3(b) and 3(c), respectively.

Figure 6: Temporal variation of (a) seismic moment, (b) static stress drop, and (c) source radius. Source parameters during the post-monsoon are shown as filled symbols. No $M_L \geq 3.5$ events occurred in the post-monsoon of 2020.

Acknowledgments

We are thankful to the Director, CSIR-NGRI, Hyderabad, for his support and permission to publish this work. Maps were plotted using the Generic Mapping Tools (Wessel and Smith, 1998). This work was carried out under CSIR-NGRI Project No. MLP-FBR-005 (MRK). The CSIR-NGRI reference number for this manuscript is NGRI/Lib/2022/Pub-97.

Author credit statement

HP: Conceptualisation, formal analysis, methodology, software, validation, visualisation, writing – original draft, writing- review and editing. **STC**.: Conceptualisation, data curation, formal analysis, methodology, software, validation, visualisation, writing - original draft. **SM**.: Investigation, data curation.

Data statement

All the waveform analyses were performed using the event waveform data, which are stored in the CSIR-NGRI repository. The waveform data can be obtained by a request to the Director, CSIR-NGRI. Daily rainfall data from the beginning of 2018 to the end of 2020, used in this study, have been obtained from the NASA repository, https://giovanni.gsfc.nasa.gov/giovanni. Supplementary Material includes Tables S1-S3 and Figures S1-S4, supporting our analysis and inferences.

Declaration of competing interests

The authors declare no competing interests

References

Aki, K. (1967). Scaling law of seismic spectrum. Journal of Geophysical Research, 72 (4),1217-1231.

Antolik, M., and Dreger, D. S. (2003). Rupture process of the 26 January 2001 M w 7.6 Bhuj, India, earthquake from teleseismic broadband data. Bulletin of the Seismological Society of America, 93(3), 1235-1248.

Baumbach, M., H. Grosser, H. G. Schmidt, A. Paulat, A. Rietbrock, C. V. Ramakrishna Rao, P. S. Raju, D. Sarkar, and I. Mohan (1994). Study of the foreshocks and aftershocks of the intraplate Latur earthquake of September 30, 1993, India, in Latur Earthquake, edited by H. K. Gupta, Mem. Geological Society of India, 35, 33– 63.

Brodsky, E. E., and Kanamori, H. (2001). Elastohydrodynamic lubrication of faults. Journal of Geophysical Research: Solid Earth, 106 (B8), 16357–16374.

Brune, J. N. (1970). Tectonic stress and the spectra of seismic shear waves from earthquakes. Journal of Geophysical Research 75(26):4997-5009.

Calais, E., Camelbeeck, T., Stein, S., Liu, M., and Craig, T. J. (2016). A new paradigm for large earthquakes in stable continental plate interiors. Geophysical Research Letters, 43(20), 10-621.

Chopra, S., Rao, K. M., Sairam, B., Kumar, S., Gupta, A. K., Patel, H., Gadhavi, M. S., and Rastogi, B. K. (2008). Earthquake swarm activities after rains in peninsular India and a case study from Jamnagar. Journal of Geological Society of India, 72(2), 245-252.

Danré, P., De Barros, L., Cappa, F., and Ampuero, J.-P. (2022). Prevalence of aseismic slip linking fluid injection to natural and anthropogenic seismic swarms. Journal of Geophysical Research: Solid Earth, 127, e2022JB025571.

De Barros, L., Cappa, F., Guglielmi, Y., Duboeuf, L., and Grasso, J. R. (2019). Energy of injection-induced seismicity predicted from in-situ experiments. Scientific Reports, 9(1), 1–11.

Dreger, D. S., Tkalčić, H., and Johnston, M. (2000). Dilational processes accompanying earthquakes in the Long Valley Caldera. Science, 288(5463), 122-125.

Earnest, A., Sunilkumar, T. C., and Silpa, K. (2021). Sinking Slab Stress and Seismo-Tectonics of the Indo-Burmese Arc: A Reappraisal. Tectonics, 40(8), e2021TC006827.

Eshelby, J. D. (1957). The determination of the elastic field of an ellipsoidal inclusion, and related problems. Proceedings of the royal society of London Series A Mathematical and Physical Sciences 241(1226):376—396.

Fischer, T., and Hainzl, S. (2017). Effective stress drop of earthquake clusters. Bulletin of the Seismological Society of America, 107(5), 2247–2257.

Gahalaut, V. K., and Singh, S. K. (2004). Fault interaction and earthquake triggering in the Koyna-Warna region, India. Geophysical Research Letters, 31(11).

Gahalaut, K., Gahalaut, V. K., Naresh, B., Shekar, M., Sunilkumar, T. C., and Srinagesh, D. (2022). Long duration non-volcanic and non-tectonic Palghar earthquake swarm in the stable continental region of India—role of seasonal rainfall and earthquake cascading. Journal of Seismology, 1-10.

Gahalaut, K., Paul, H., Sunilkumar T.C., Ravi Kumar, M., and Gahalaut, V. K. (2023). Earthquakes induced by rapid loading of faults during Pulichintala reservoir impoundment in the stable continental region of India, Earth and Space Science, 10, e2023EA002902.

Gupta, H. K. (2002). A review of recent studies of triggered earthquakes by artificial water reservoirs with special emphasis on earthquakes in Koyna, India. Earth-Science Reviews, 58(3-4), 279-310.

Hainzl, S., Kraft, T., Wassermann, J., Igel, H., and Schmedes, E. (2006). Evidence for rainfall-triggered earthquake activity. Geophysical Research Letters, 33(19).

Hainzl, S., Aggarwal, S. K., Khan, P. K., and Rastogi, B. K. (2014). Monsoon-induced earthquake activity in Talala, Gujarat, India. Geophysical Journal International, 200(1), 627-637.

Hardebeck, J. L., and Hauksson, E. (2001). Crustal stress field in southern California and its implications for fault mechanics. Journal of Geophysical Research: Solid Earth, 106(B10), 21859-21882.

Herrmann, R. B. (2013). Computer programs in seismology: An evolving tool for instruction and research. Seismological Research Letters, 84(6), 1081-1088.

Hill, D. P. (1977). A model for earthquake swarms. Journal of Geophysical Research, 82(8), 1347-1352.

Husen, S., C. Bachmann, and D. Giardini (2007), Locally triggered seismicity in the central Swiss Alps following the large rainfall event of August 2005, Geophysical Journal International, 171, 1126–1134.

Hutton, L. K., and Boore, D. M. (1987). The ML scale in southern California. Bulletin of the Seismological Society of America, 77(6), 2074-2094.

Johnston, A. C. (1996). Seismic moment assessment of earthquakes in stable continental regions—II. Historical seismicity. Geophysical Journal International, 125(3), 639-678.

Kanamori, H., and Rivera, L. (2004). Static and dynamic scaling relations for earthquakes and their implications for rupture speed and stress drop. Bulletin of the Seismological Society of America, 94 (1), 314–319.

Kanaujia, J., Kumar, M. R., Vengala, P. K., and Shekar, M. (2025). Indication of fluid-driven seismicity in the Palghar region, India, from local earthquake tomography. Bulletin of the Seismological Society of America, 115 (2), 489–504.

Kulkarni, A. (2012). Weakening of Indian summer monsoon rainfall in warming environment. Theoratical and Applied Climatology, 109, 447–459.

Lomax, A., Virieux, J., Volant, P., and Berge-Thierry, C. (2000). Probabilistic earthquake location in 3D and layered models. In Advances in seismic event location, pp. 101-134. Springer, Dordrecht.

Lohman, R. B., and McGuire, J. J. (2007). Earthquake swarms driven by aseismic creep in the Salton Trough, California. Journal of Geophysical Research: Solid Earth, 112(B4).

Mahato, C. (2024). Stress drops and scaled energies of micro-earthquakes at Koyna-Warna, India: Implications for self-similarity scaling. Journal of Asian Earth Sciences, 263, 106042.

Michael, A. J. (1984). Determination of stress from slip data: faults and folds. Journal of Geophysical Research: Solid Earth, 89(B13), 11517-11526.

Mogi, K. (1963) Magnitude-frequency relation for elastic shocks accompanying fractures of various materials and some related problems in earthquakes (2nd paper). Bulletin of the Earthquake Research Institute, University of Tokyo 40(4):831-853.

Nur, A., and Simmons, G. (1969). The effect of saturation on velocity in low porosity rocks. Earth and Planetary Science Letters, 7 (2), 183–193.

Paul, H., Mitra, S., Bhattacharya, S. N. and Suresh, G. (2015). Active transverse faulting within underthrust Indian crust beneath the Sikkim Himalaya. Geophysical Journal International, 201, 1080-1081, doi: 10.1093/gji/ggv058.

Paul, H., Ravi Kumar, M. and Kumar, S. (2021). Evidence for reactivation of new faults and seismicity migration away from the causative fault of the 2001 M_W 7.7 Bhuj earthquake, western India. Geophysical Journal International, 226, 1800-1813.

Paul, H., Sunilkumar, T. C., Gahalaut, V. K., Srinagesh, D., and Shekar, M. (2024). Significance of V_P/V_S ratio in locating earthquakes of a long-duration swarm in the western coast of India. Journal of Seismology, **28(3)**, 859-877.

Paul, H., Sunil Kumar, T. C., Naresh, B., and Ravi Kumar, M. (2025). Minor lithospheric mantle earthquakes beneath the South Indian Shield: Implications for continental mantle rheology. Journal of Geophysical Research: Solid Earth, 130, e2025JB031522.

Paul, H. and Shekar, M. (2026). Stress triggering in a rain-induced earthquake swarm in the Palghar region, western India. Scientific Reports (under review).

Popp, T., and Kern, H. (1994). The influence of dry and water saturated cracks on seismic velocities of crustal rocks-a comparison of experimental data with theoretical model. Surveys in Geophysics, 15 (5), 443–465.

Rajendran, K., Parameswaran, R. M., and Rajendran, C. P. (2017). Seismotectonic perspectives on the Himalayan arc and contiguous areas: Inferences from past and recent earthquakes, Earth-Science Reviews, 173, 1-30.

Raju, P. S., Srinivasan, A., Raghavan, R. V., and Kousalya, M. (2000). Micro-tremor activity in Jubilee hills area of Hyderabad, Andhra Pradesh. Journal of Geological Society of India (Online archive from Vol 1 to Vol 78), 55(4), 443-445.

Rao, D. T., Jambusaria, B. B., Srivastava, S., Srivastava, N. P., and Hamid, A. (1991). Earthquake swarm activity in south Gujarat. Mausam (New Delhi), 42(1), 89-98.

Sateesh, A., Mahesh, P., Singh, A. P., Kumar, S., Chopra, S., and Kumar, M. R. (2019). Are earthquake swarms in South Gujarat, northwestern Deccan Volcanic Province of India monsoon induced? Environmental Earth Sciences, 78(13), 1-13.

Satriano, C. (2023). SourceSpec – Earthquake source parameters from P- or S-wave displacement spectra (1.6). https://doi.org/10.5281/ZENODO.3688587.

Shapiro, S. A., Huenges, E., and Borm, G. (1997). Estimating the crust permeability from fluid-injection-induced seismic emission at the KTB site. Geophysical Journal International, 131(2), F15-F18.

Sharma, V., Wadhawan, M., Rana, N., Sreejith, K. M., Agrawal, R., Kamra, C., Hosalikar, K., Narkhede, K.V., Suresh, G., and Gahalaut, V. K. (2020). A long duration non-volcanic earthquake sequence in the stable continental region of India: The Palghar swarm. Tectonophysics, 779, 228376.

Sharma, V., Kumar, D., Sharma, B. and Chingtham, P. (2023). Characteristics of earthquake swarm activity observed in the Palghar region of Indian Peninsula from January 2019 to October 2020, Quaternary Science Advances, 12, 100099.

Shelly, D. R., Hill, D. P., Massin, F., Farrell, J., Smith, R. B., and Taira, T. A. (2013). A fluid-driven earthquake swarm on the margin of the Yellowstone caldera. Journal of Geophysical Research: Solid Earth, 118(9), 4872–4886.

Sibson, R. H. (2003). Brittle-failure controls on maximum sustainable overpressure in different tectonic regimes. AAPG Bulletin, 87(6), 901–908.

Simpson, R. W. (1997). Quantifying Anderson's fault types. Journal of Geophysical Research: Solid Earth, 102(B8), 17909–17919.

Singh, A. P., and Mishra, O. P. (2015). Seismological evidence for monsoon induced micro to moderate earthquake sequence beneath the 2011 Talala, Saurashtra earthquake, Gujarat, India. Tectonophysics, 661, 38–48.

Singh, A. P., Pandey, P., Tomar, Y. S., Singh, N. K. and Mishra, O. P. (2026). Seismic velocity structure and crack attributes in focal area of earthquake swarm beneath the Deccan Volcanic Province, Western India. Physics of the Earth and Planetary Interiors, 372, 107517.

Srinagesh, D., Singh, D. K., Vikas, G., Naresh, B., Roy, S., Murthy, Y., Raju, P.S., Suresh, G., Mandal, P., Sharma, A. N. S. and Tiwari, V. M. (2020). An appraisal of recent earthquake activity in Palghar region, Maharashtra, India. Current Science, 118(10), 1592.

Srivastava, H. N., and Dube, R. K. (1996). Comparison of precursory and non-precursory swarm activity in peninsular India. Tectonophysics, 265(3-4), 327–339.

Subhadra, N, and M. Shekar (2024). The attenuation mechanism of high-frequency seismic waves in the Palghar swarm earthquake source area in Western India, Journal of Asian Earth Sciences, 276, 106306.

Sunilkumar, T., Earnest, A., Silpa, K., and Andrews, R. (2019). Rupture of the Indian slab in the 2011 Mw 6.9 Sikkim Himalaya earthquake and its tectonic implications. Journal of Geophysical Research: Solid Earth, 124 (3), 2623–2637.

Talwani, P., Chen, L., and Gahalaut, K. (2007). Seismogenic permeability, ks. Journal of Geophysical Research: Solid Earth, 112(B7).

Vavryčuk, V. (2011). Principal earthquakes: Theory and observations from the 2008 West Bohemia swarm. Earth and Planetary Science Letters, 305(3-4), 290–296.

Vavryčuk, V. (2014). Iterative joint inversion for stress and fault orientations from focal mechanisms. Geophysical Journal International, 199 (1), 69–77.

Vavryčuk, V. (2015). Moment tensor decompositions revisited. Journal of Seismology, 19(1), 231–252.

Wadhawan, M., Rana, N., Gahalaut, V., Singh, M., Singh, K., Suresh, G., Mishra, O. P., Joshi, A. K., Kulkarni, A. V., Singh, M., Das, A. K., (2021). Monsoonal rainfall induced shallow earthquake Swarm in the Amravati district of the central India. Journal of Earth System Science, 130(1), 1–7.

Wessel, P., and Smith, W. H. (1998). New, improved version of Generic Mapping Tools released. Eos, Transactions American Geophysical Union, 79(47), 579–579.

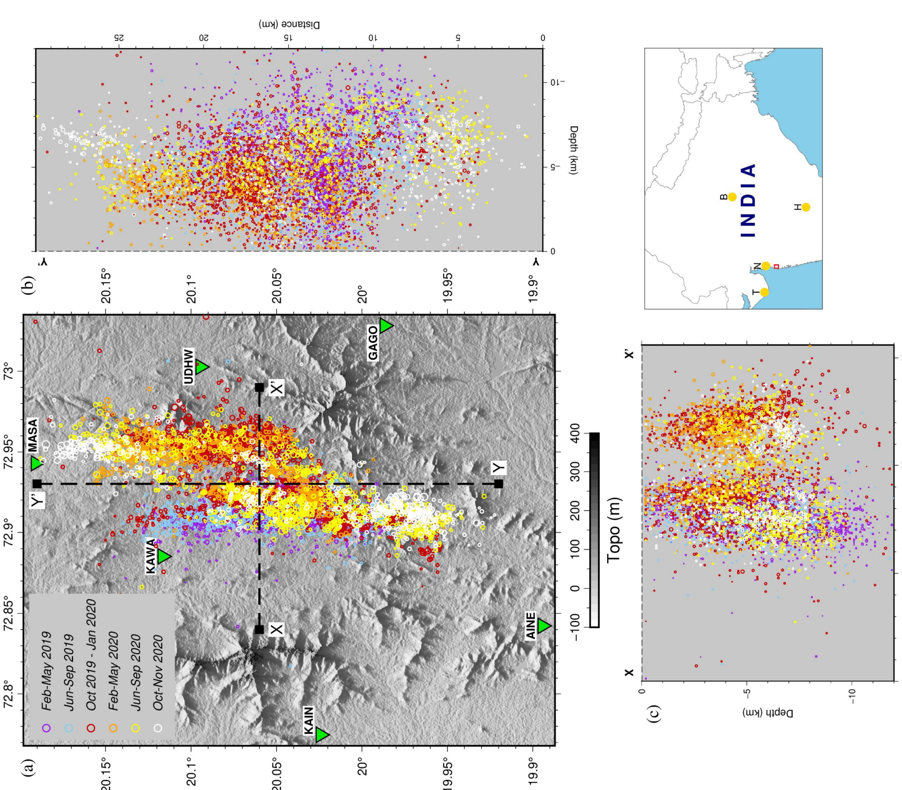

Figure 1. Plot of the Palghar seismicity in (a) map view, (b) cross-section along the N-S profile Y-Y' and (c) cross-section along the E-W profile X-X'. The seismicity is colour-coded by time, with each colour representing approximately 4-months of activity. In (a), seismic stations are shown as green triangles. The inset map of India is displayed in the lower right. Locations of a few past swarms within India are shown as yellow ovals in the inset and labelled. N-Navsari, T-Talala, B-Bamhori, H-Hyderabad. The red square represents the study region.

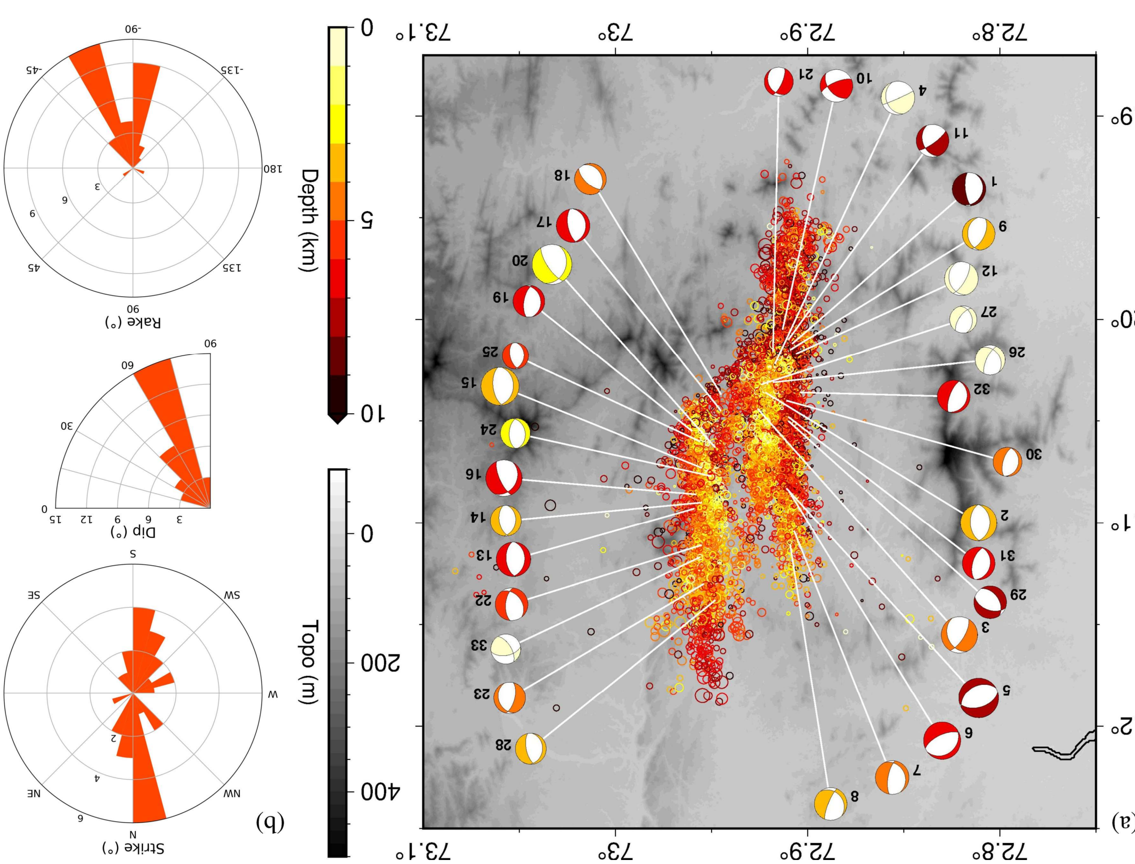

Figure 2. (a) Double-couple focal mechanisms of the Palghar swarm, along with seismicity, are shown on the topography map. Both seismicity and focal mechanisms are colour-coded by depth. Serial numbers corresponding to the focal mechanism solutions in Table S1 (Supplementary) are labelled beside the beach-ball diagrams. (b) Rose-plot distributions of strike, dip and rake from the focal mechanism solutions are shown.

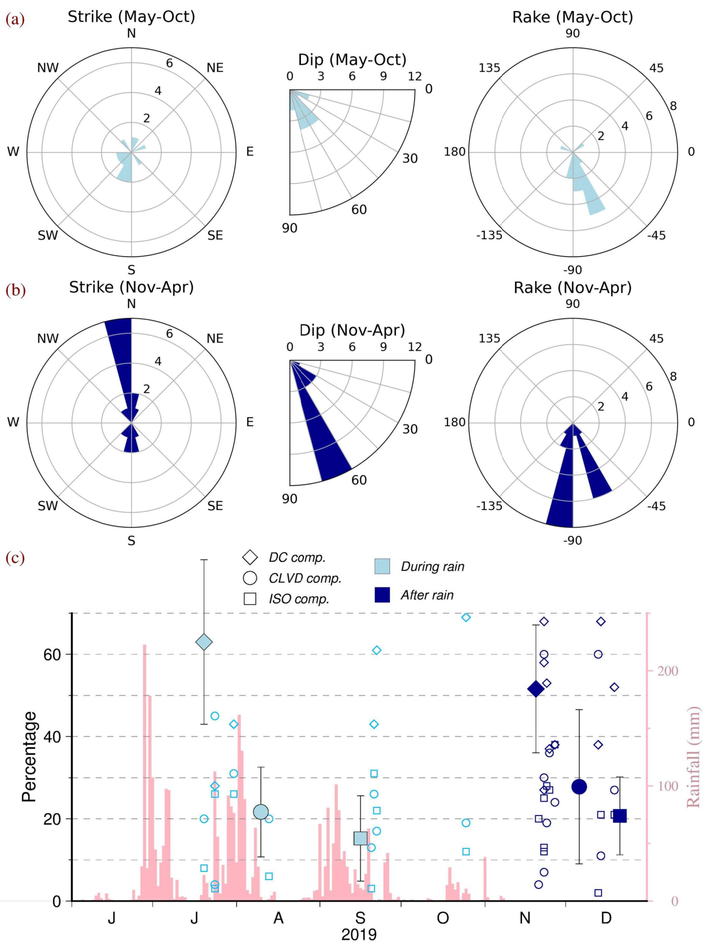

Figure 4. : Rose-plot distributions of strike, dip and rake from focal mechanisms during (a) May to October and (b) November to April. (c) Plot of the double-couple (DC, diamond symbol), compensated linear vector dipole (CLVD, circle), and isotropic (ISO, square) components of the focal mechanism solutions as a function of time (June to December 2019). Individual values are shown as open symbols, while mean values (with standard deviation) are larger filled symbols. Quantities during summer (including monsoon) are indicated in sky blue, whereas those during the post-monsoon are in deep blue. The x-positions of the mean values are unrelated to time and are plotted in this way for visual convenience. Daily rainfall (obtained from the NASA repository, https://giovanni.gsfc.nasa.gov/giovanni) is plotted as pink histograms.

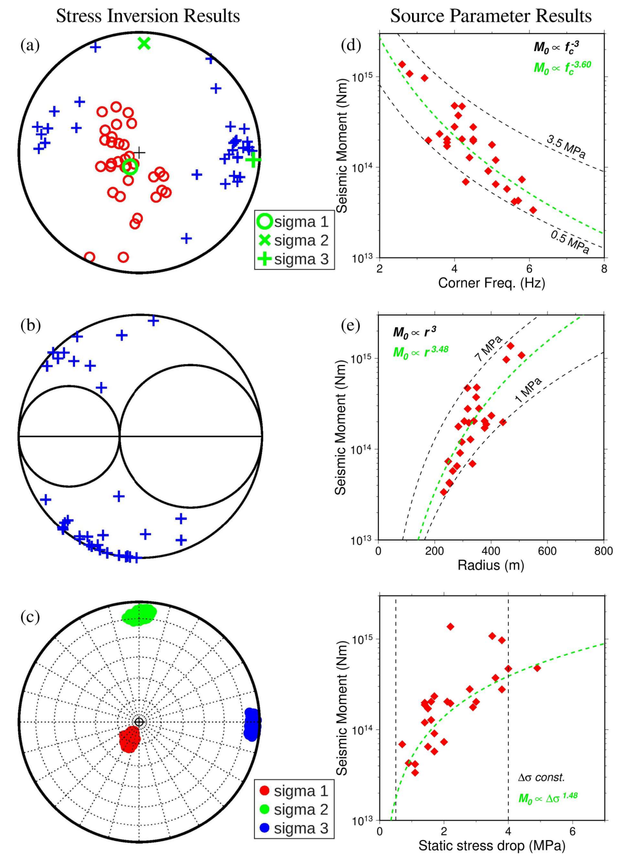

Figure 3. Stress inversion and source parameter results obtained from all $M_L \geq 3.5$ earthquakes of the Palghar swarm. (a) Azimuthal plot of Pressure- (red circles) and Tension-axes (blue + symbols) from focal mechanisms, shown along with the orientation of principal stresses, (b) 3D Mohr circle representation of the principal stresses, with normal stress increasing along the x-axis and shear stress increasing along the y-axis. The diameter of the large circle is σ_1 - σ_3, and the two inner circles meet at σ_2, where σ_1, σ_3, and σ_2 are the maximum, minimum and intermediate principal stresses. The blue + symbols represent individual nodal planes. (c) Inverted principal stress axes (with 95% confidence interval) shown in lower-hemisphere projection. Plots of (d) corner frequency vs seismic moment, (e) source radius vs seismic moment, and (f) static stress drop vs seismic moment are shown as red diamond symbols. Dashed black lines in (d), (e) and (f) represent scale-invariance for fixed static stress drops, whereas dashed green lines represent scale-dependence.

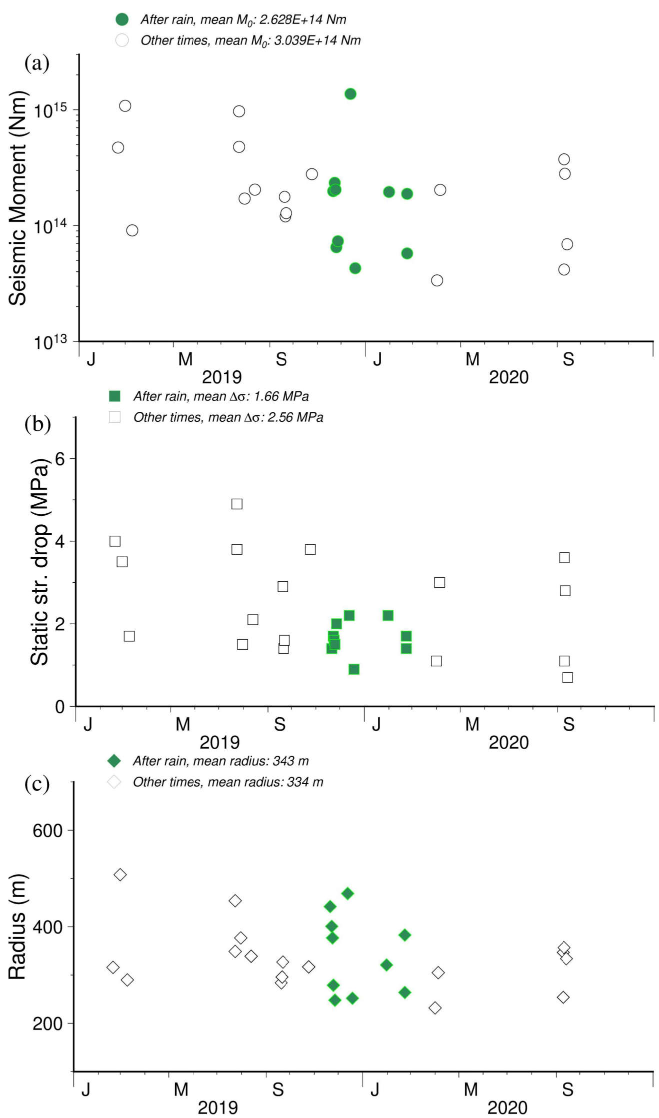

Figure 6. Temporal variation of (a) seismic moment, (b) static stress drop, and (c) source radius. Source parameters during the post-monsoon are shown as filled symbols. No $M_L \geq 3.5$ events occurred in the post-monsoon of 2020.

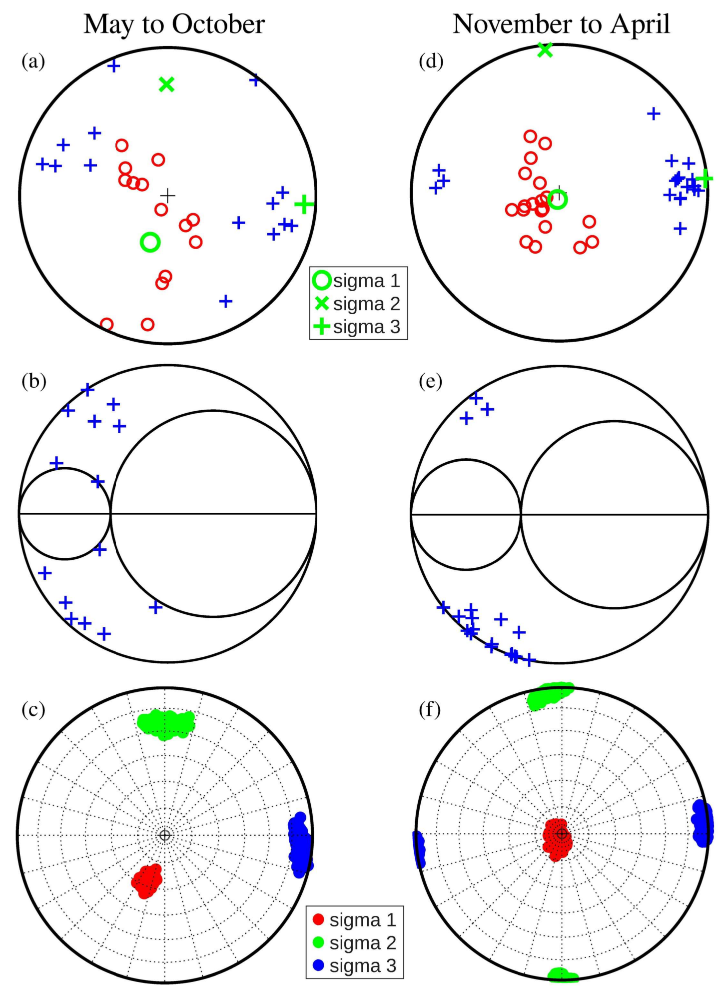

Figure 5. Stress inversion results separated for focal mechanisms during May to October and November to April. (a), (d) Azimuthal plots of P- and T-axes, along with the orientation of principal stresses. (b), (e) 3D Mohr circle representations of the principal stresses. (c), (f) Inverted principal stress axes (with 95% confidence interval) shown in lower-hemisphere projection. For interpretation of the various colours and symbols, refer to the captions of Fig. 3(a), 3(b) and 3(c), respectively.